Applied Catalysis B: Environmental 325 (2023) 122320

Contents lists available at ScienceDirect

Applied Catalysis B: Environmental

journal homepage: www.elsevier.com/locate/apcatb

Unravelling the active sites and structure-activity relationship on Cu–ZnO–Al_2O_3 based catalysts for water-gas shift reaction

Seon-Yong Ahn [a], Kyoung-Jin Kim [a], Beom-Jun Kim [a], Jae-Oh Shim [b], Won-Jun Jang [c,*], Hyun-Seog Roh [a,*]

[a] Department of Environmental and Energy Engineering, Yonsei University, 1 Yonseidae-gil, Wonju-si, Gangwon-do 26493, South Korea
[b] Department of Chemical Engineering, Wonkwang University, 460 Iksan-daero, Iksan-si, 54538 Jeollabuk-do, South Korea
[c] Department of Environmental and Energy Engineering, Kyungnam University, 7 Kyungnamdaehak-ro, Changwon-si, 51767 Gyeongsangnam-do, South Korea

ARTICLE INFO

Keywords:
Water gas shift
Hydrogen production
Cu–ZnO–Al_2O_3
Structure insensitivity
Cu content
Cu^+

ABSTRACT

Herein, we investigated the main active sites and structure-sensitivity of the water-gas shift (WGS) reaction over ternary Cu–ZnO–Al_2O_3 (CZA) catalysts. CZA catalysts with various Cu contents were synthesized by the homogeneous one-step coprecipitation method. The Cu content mainly affected the number of active Cu sites and was closely related to the WGS activity. Turnover frequency (TOF) values were independent of Cu dispersion, indicating that the CZA catalyst is structure-insensitive in WGS. The ratio of surface Cu^+ species also strongly influenced the activity of the CZA catalyst. TOF based on the total active Cu species showed a constant value, but the CO conversion was linearly increased with the number of surface Cu^+ species.

1. Introduction

The recent economic downturn caused by COVID-19 has accelerated the severity of energy-related environmental issues, and annual CO_2 emissions have risen sharply as the rebounding growth engine relies on coal-based fuels. In addition, energy-related CO_2 emissions (36.3 Gt) in 2021 hit the second highest level in post-industrial history, as global industrial production activity recovers and transportation demand increases. To overcome this situations, integrated approaches are emerging as the energy sector on the verge of transformation, driven by technological progress such as electrification, decarbonization, sustainable energy resources and CO_2 capture and storage (CCS) and utilization (CCU) [1]. Hydrogen is a strong candidate among the technologies to secure sustainable and clean energy. In this regard, the major countries represented by the United States, Japan and Germany have set hydrogen economy construction as a key strategy and are implementing the national project. WGS ($CO + H_2O \rightarrow CO_2 + H_2$) is a crucial process for hydrogen production and syngas purification [2–4]. Binary Cu–ZnO and ternary CZA systems have been widely utilized as commercial catalysts in WGS. However, there are still controversies concerning the exact active species, reaction mechanism and structure-sensitivity of WGS. In particular, since CZA catalysts employ Cu as an active metal, which is vulnerable to thermal stress and is significantly affected by reaction conditions such as an oxidizing atmosphere, it is difficult to study clearly. Ginés et al. [5] investigated the structure-activity relationship of CZA system in WGS. The specific reaction rate was proportional to the metallic Cu surface area and irrespective of the A1/Zn ratio, Cu crystallite size, and Cu contents, thereby suggesting that WGS is structure-insensitive over CZA system.

Yan et al. [6] studied the Cu-Fe_3O_4 catalysts with different Cu-Fe molar ratio to solve the deactivation problem of Cu based catalysts due to the sintering, CO poisoning, or limited Cu^0. They found that optimization of Cu contents was important to control WGS activity for Cu-Fe_3O_4 catalyst.

Cui and co-workers [7] developed the Al_2O_3 supported Cu catalysts containing dual sites of Cu^+ single atoms and Cu^0 nanoparticles. The synergetic effect of dual sites helps to increase surface CO concentration as well as to prevent competitive CO adsorption on Cu^0 nanoparticles sites with H_2O, improving the catalytic performance.

Zhang et al. [8] found that $Cu_{Cu(100)}$-hydroxylated ZnO ensembles was active sites of ZnO/Cu catalysts for WGS reaction. The active sites are formed by Cu structure-dependent and reaction-sensitive *in-situ* restructuring.

In this paper, to achieve more insight into the relationship between the activity and the physicochemical properties of the catalyst, we have studied the structure-sensitivity of WGS over CZA catalysts. To reveal

* Corresponding authors.
E-mail addresses: wjjang@kyungnam.ac.kr (W.-J. Jang), hsroh@yonsei.ac.kr (H.-S. Roh).

https://doi.org/10.1016/j.apcatb.2022.122320
Received 31 October 2022; Received in revised form 18 December 2022; Accepted 20 December 2022
Available online 22 December 2022

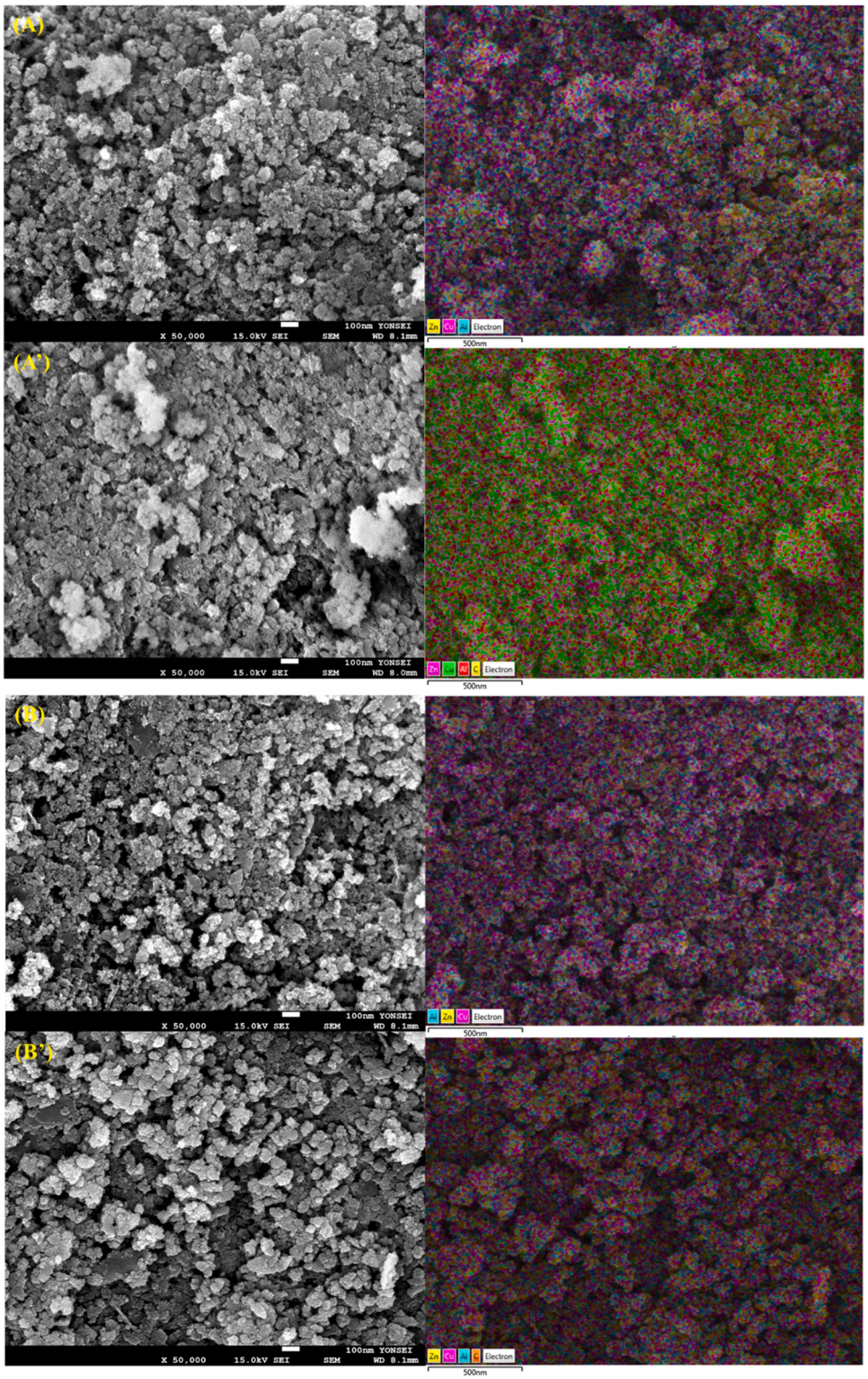

Fig. 1. SEM-EDS mapping results of reduced and used CZA catalysts depending on Cu contents: (A) reduced 70Cu20Zn10Al, (A′) used 70Cu20Zn10Al, (B) reduced 65Cu25Zn10Al, (B′) used 65Cu25Zn10Al, (C) reduced 60Cu30Zn10Al, (C′) used 60Cu30Zn10Al, (D) reduced 50Cu40Zn10Al, (D′) used 50Cu40Zn10Al, (E) reduced 65Cu35Zn, (E′) used 65Cu35Zn, (F) reduced 65Cu35Al, and (F′) used 65Cu35Al.

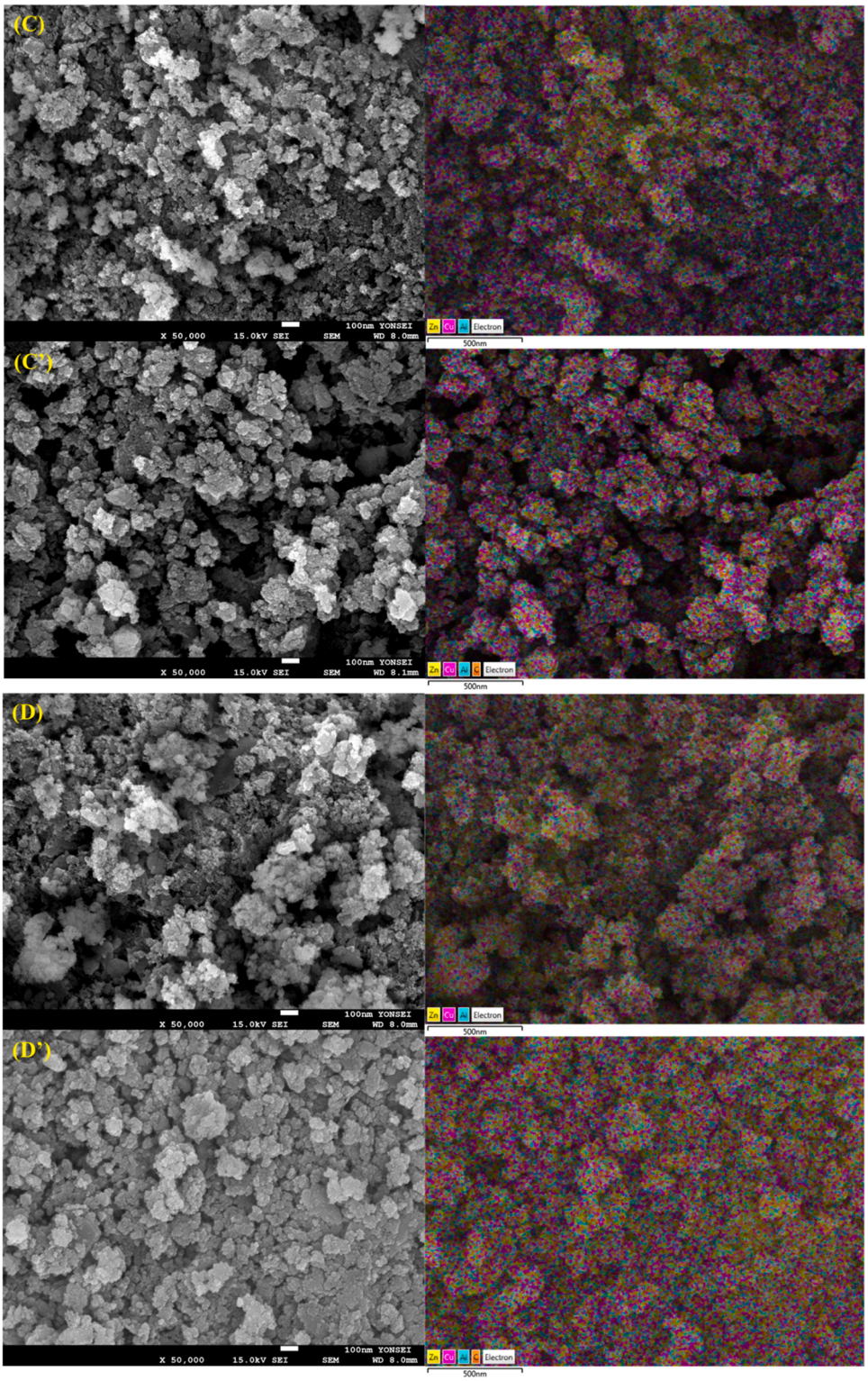

Fig. 1. (*continued*).

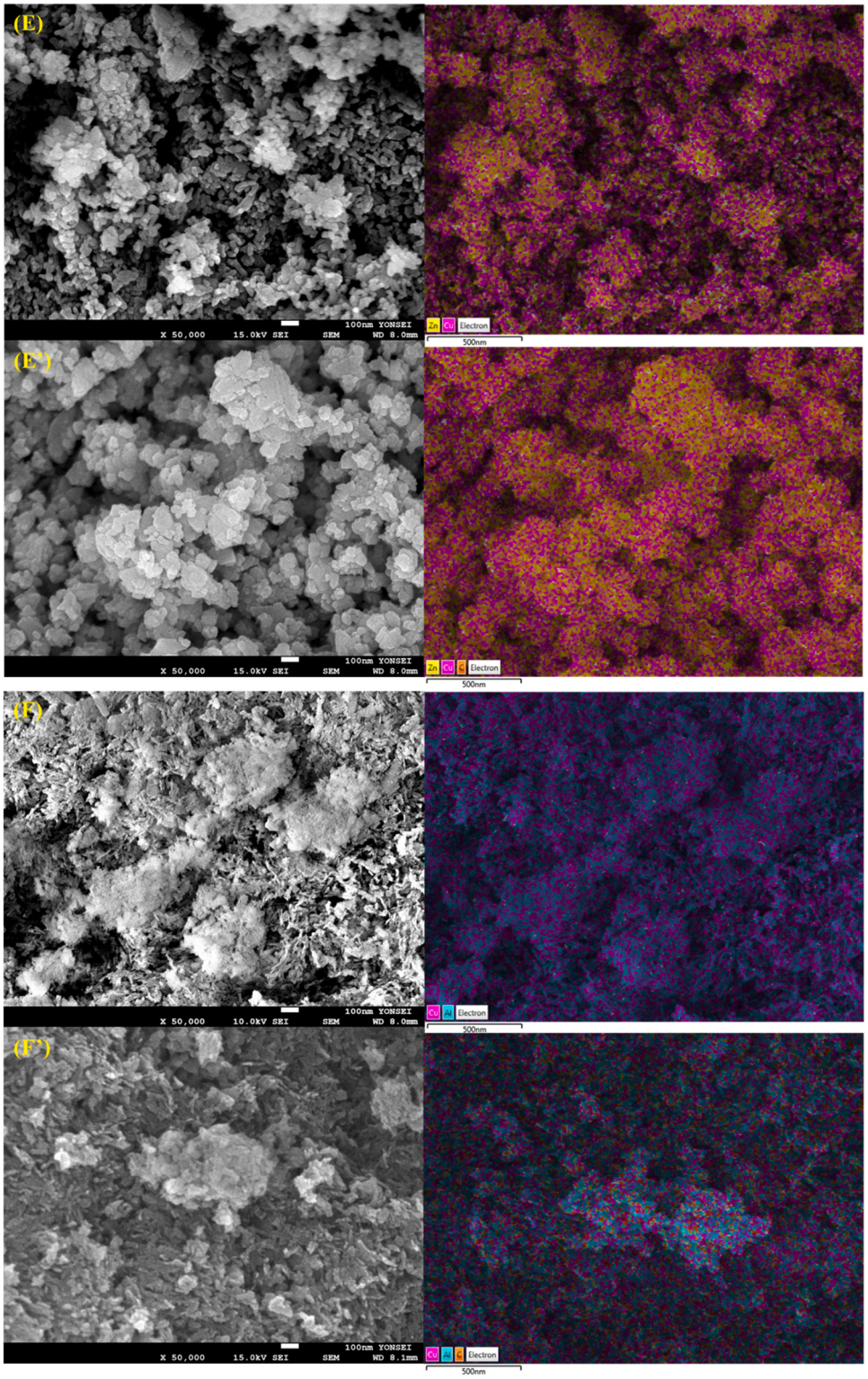

Fig. 1. (*continued*).

the active sites and structure-activity relationship on the CZA catalyst, TOF was systematically measured with various Cu contents.

2. Experimental

2.1. Catalyst preparation

$Cu–ZnO–Al_2O_3$ catalysts with various Cu contents (50, 60, 65 and 70 wt.%) were synthesized by the homogeneous one-step coprecipitation method using $Cu(NO_3)_2{\cdot}xH_2O$ (99.999 %, Sigma–Aldrich), $Zn(NO_3)_2{\cdot}6H_2O$ (98 %, Sigma–Aldrich), and $Al(NO_3)_3{\cdot}9H_2O$ (98 %, Sigma–Aldrich). KOH (95 %, Samchun Chemicals) was used as the precipitating agent. The Al content was fixed at 10 wt.%, and Zn content (20–40 wt.%) varied depending on the Cu content. Following the dissolution of stoichiometric quantities of precursors in 100 mL of deionized water, a 2.7 M KOH solution was injected into the precursor

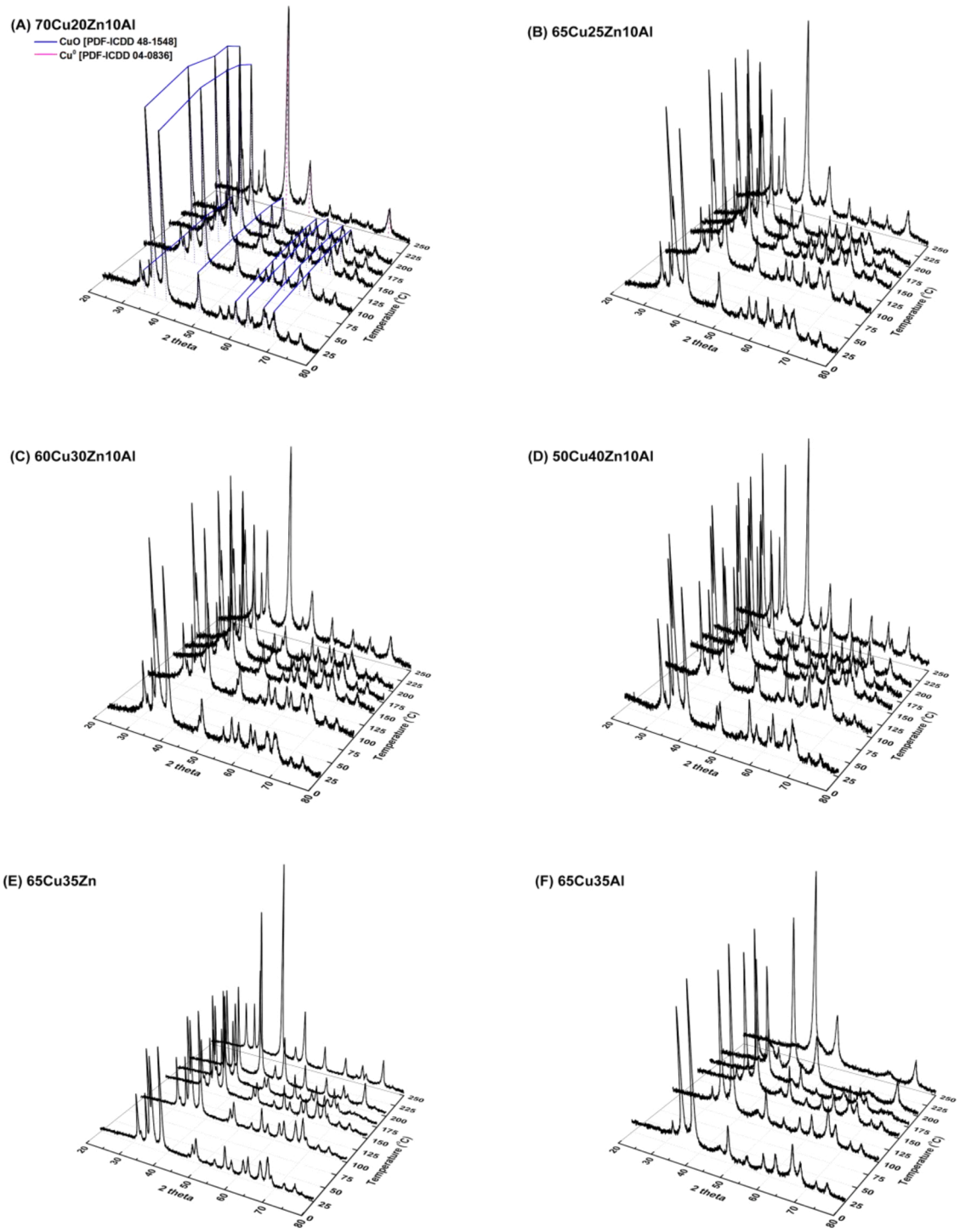

Fig. 2. *In-situ* XRD patterns of CZA catalysts depending on Cu contents.

solution at an injection rate of 30 mL/min at 80 °C with constant stirring. The precipitation solution was aged at 80 °C for 72 h. After the aging procedure, the solution with precipitate was washed several times with deionized water, and the precipitate was filtered off using filter paper (Cat. No. 1005–110, Whatman). Then the extracted solid precipitate was dried at 110 °C for 10 h, and calcined at 400 °C for 6 h in an air atmosphere to obtain the catalyst. The synthesized catalysts were labeled as follows according to the Cu content: 70Cu20Zn10Al (Cu loading = 70 wt.%), 65Cu25Zn10Al (Cu loading = 65 wt.%), 60Cu30Zn10Al (Cu loading = 60 wt.%), and 50Cu40Zn10Al (Cu loading = 50 wt.%). To further investigate the Cu behavior by support material, Cu–ZnO (labeled as 65Cu35Zn; Cu, Zn loading = 65, and 35 wt.%, respectively) and Cu–Al_2O_3 (labeled as 65Cu35Al; Cu, Al loading = 65, and 35 wt.%, respectively) catalysts were synthesized using the same method above.

2.2. Characterization

N_2 adsorption/desorption isotherms at −196 °C using an ASAP 2010 apparatus (Micromeritics) were applied to determine specific surface areas and to investigate the pore structure. To remove impurities and residual gas components in the sample, samples were degassed for 12 h

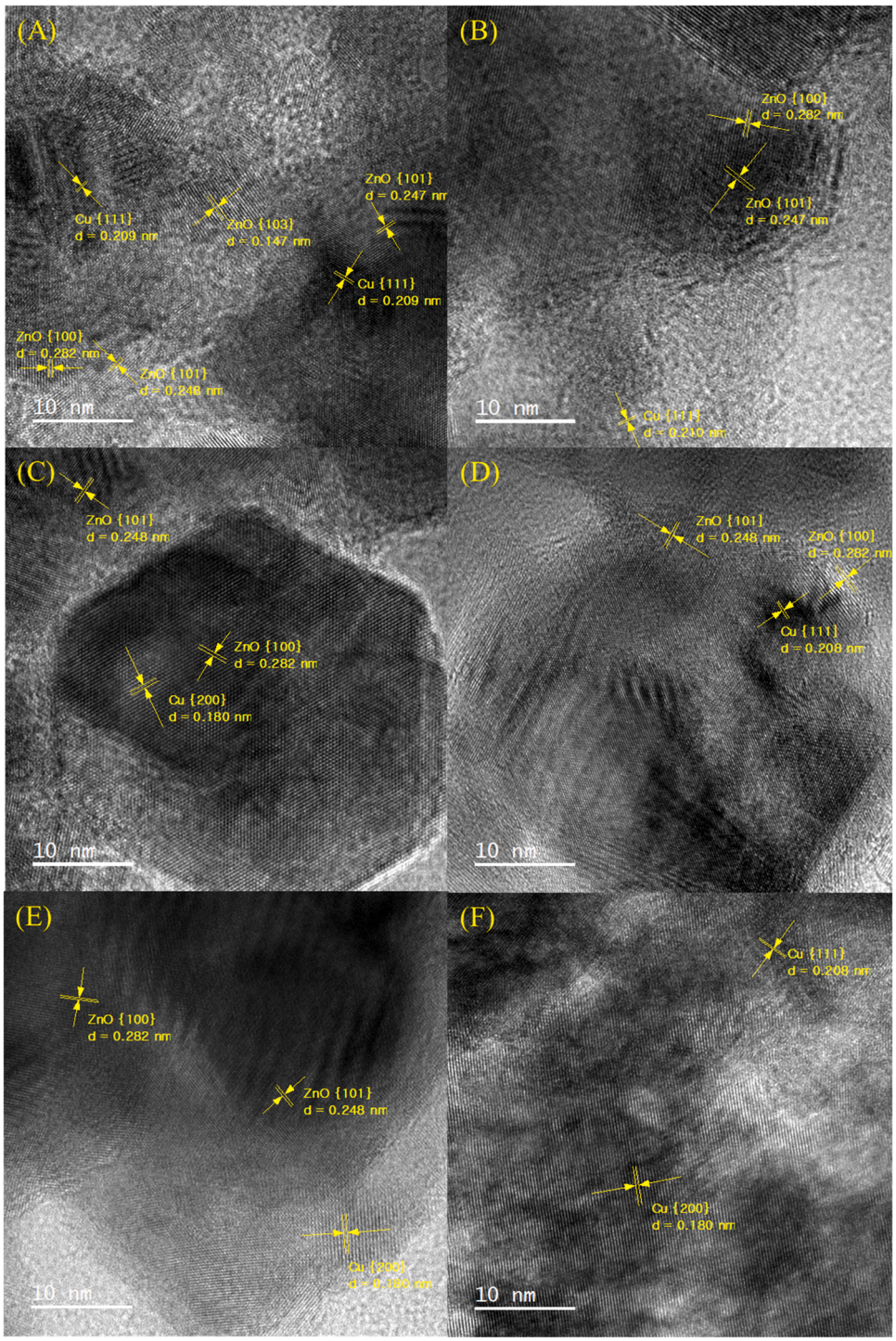

Fig. 3. HR-TEM images of reduced CZA catalysts with various Cu contents: (A) 70Cu20Zn10Al, (B) 65Cu25Zn10Al, (C) 60Cu30Zn10Al, (D) 50Cu40Zn10Al, (E) 65Cu35Zn, and (F) 65Cu35Al.

at 110 °C in a vacuum less than 0.5 mmHg. N_2O-titration was conducted using an Autochem II 2920 (Micromeritics) device. Prior to the titration of N_2O, 0.1 g of the sample was reduced *in-situ* in a 2 % H_2/Ar atmosphere at 250 °C for 1 h and then cooled to 60 °C in an Ar atmosphere. N_2O consumption and N_2 emission ($N_2O + 2Cu \rightarrow Cu_2O + N_2$) at metal Cu sites were estimated using a thermal conductivity detector by injecting 5 % N_2O/He gas at 60 °C with a pulse. ($[N_2O / Cu_s] = 0.5$). *In-situ* X-ray diffraction (*in-situ* XRD) analysis was carried out in the temperature range of 25–250 °C with a rate of 3.3 °C/min in 2 vol.% H_2/N_2 atmosphere using an X'Pert PRO (Cu-Kα radiation, 40 kV, 30 mA, Malvern PANalytical Ltd.) instrument with a scanning speed of 2°/min. Temperature programmed reduction (TPR) analysis was performed at room temperature up to 500 °C at 10 °C/min in a 10 % H_2/Ar atmosphere using an Autochem II 2920 (Micromeritics) apparatus to investigate the reduction properties of the catalysts. X-ray photoelectron spectroscopy (XPS) analysis was conducted using an Al–Kα spectrophotometer (Thermo-Scientific) equipped with a high-resolution monochromator. The detector was maintained at 100 and 50 eV pass energy modes for the measurement of survey spectra and detailed spectra, respectively. Binding energies were calibrated using the C 1s

Table 1
Characteristics of CZA catalysts depending on Cu contents.

Catalyst	S.A. (m^2/g)[a]	Cu dispersion (%)[b]	Metal S.A. (m^2/g)[b]	Cu particle size (nm)[b]	Number of Cu surface atoms (10^{19} atoms/g_{cat})
70Cu20Zn10Al	76.2	1.12	7.22	77.6	5.94
65Cu25Zn10Al	60.7	1.12	7.20	77.9	5.49
60Cu30Zn10Al	71.1	0.95	6.10	91.8	4.30
50Cu40Zn10Al	64.4	0.89	5.71	98.2	3.35
65Cu35Zn	25.5	0.42	2.69	208.7	2.05
65Cu35Al	138.9	0.55	3.53	158.7	2.70

[a] Estimated from N_2 adsorption at −196 °C.
[b] Estimated from N_2O-titration (pre-reduction at 250 °C for 1 h in 2 % H_2/Ar atmosphere).

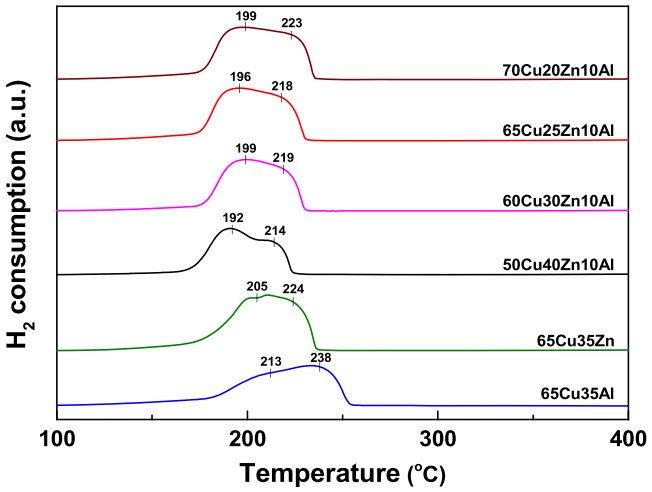

Fig. 4. TPR patterns of CZA catalysts depending on Cu contents.

transition peak centered at 284.6 eV. Cu K-edge XANES (X-ray absorption near-edge structure) and EXAFS (extended X-ray absorption fine-structure) spectra were recorded at the 1C Tr-XAS beamline located in the Pohang Accelerator Laboratory (PAL), Republic of Korea. XANES and EXAFS spectra were collected in the transmission mode for Cu K-edge. Data reducing was conducted using Athena and Artemis software (Demeter) with the FEFF8 code. The raw data were smoothed, background-removed, and normalized. After data reducing and normalization of atomic absorption, the $k^3\chi$ (k)-weighted EXAFS spectra were Fourier transformed to R space in the k range from 2.5 to 13.0 $Å^{-1}$ using the first shell theoretical scattering amplitudes. High resolution-transmission electron microscopy (HR-TEM) images and energy dispersive X-ray spectroscopy (EDS) of the synthesized catalysts were collected using a JEM-F200 (JEOL Ltd.) microscope with a 200 kV operating voltage. All the samples were suspended in ethanol by ultra-sonication, and the prepared suspension was deposited on a copper grid with a carbon film for TEM measurement. Scanning electron microscopy (SEM) was carried out using a JSM-7610 F Plus (JEOL Ltd.) operating at 15 kV.

2.3. Catalytic reaction

The LT-WGS reaction was conducted in a fixed-bed microtubular quartz reactor (I.D.: 4 mm) packed with quartz wool at atmospheric pressure. For intrinsic activity tests, 100 mg of powder type catalyst was loaded on the quartz wool, and a K-type thermocouple was inserted in the middle of the catalyst bed to check the actual temperature during the reaction. The catalyst was physically mixed with SiO_2 (acid washed, Sigma–Aldrich) at a SiO_2/catalyst ratio between 1 and 7.5 (wt/wt). To

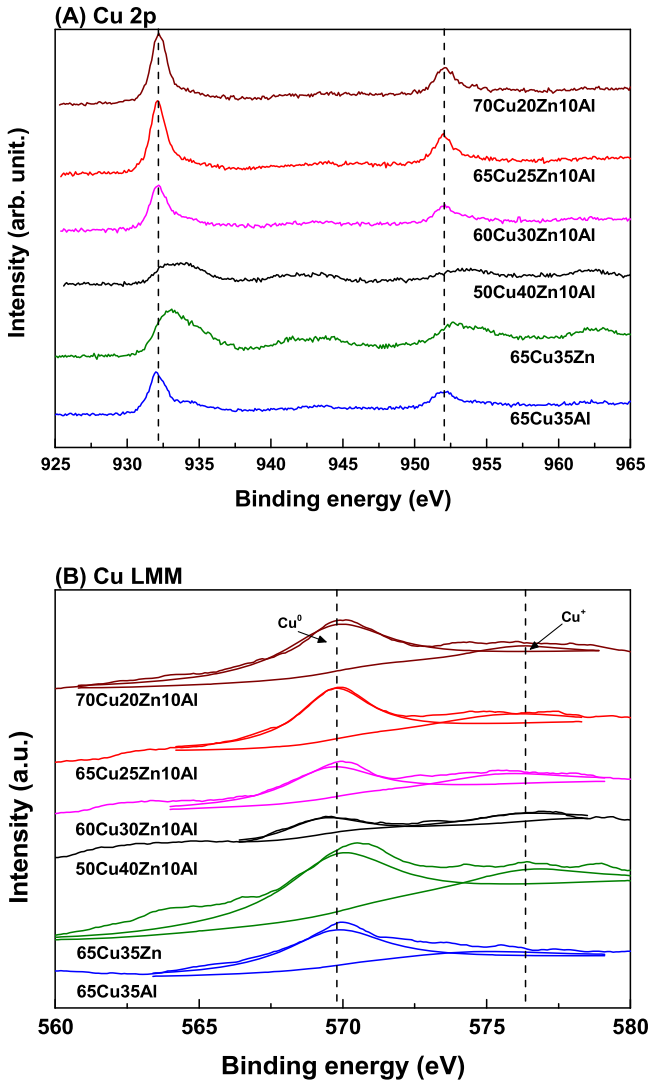

Fig. 5. XPS spectra of reduced CZA catalysts depending on Cu contents: (A) Cu 2p, and (B) Cu LMM.

Table 2
Surface atomic ratios of CZA catalysts depending on Cu contents.

Catalyst	Cu^+/ (Cu^+ + Cu^0)	Number of Cu^+ surface atoms (10^{19} atoms/g_{cat})[a]
70Cu20Zn10Al	0.25	1.49
65Cu25Zn10Al	0.35	1.92
60Cu30Zn10Al	0.31	1.33
50Cu40Zn10Al	0.30	1.01
65Cu35Zn	0.30	0.62
65Cu35Al	0.28	0.77

[a] Number of Cu^+ surface atoms = Number of Cu surface atoms (10^{19} atoms/g_{cat}) × Cu^+ fraction.

activate the catalyst before injecting the reaction gas, the temperature of the catalyst bed was raised from room temperature to 250 °C in a 2 vol. % H_2/N_2 atmosphere at a rate of 3.3 °C/min, and then maintained for 1 h. After the activation step was completed, the temperature of the catalyst bed was set to 200 °C and cooled for 30 min. Under this condition, the LT-WGS reaction was performed by continuously injecting the reactant gas (H_2: 60.0 vol.%, N_2: 20.0 vol.%, CH_4: 1.0 vol.%, CO: 9.0 vol.%, and CO_2: 10.0 vol.%) using a mass flow controller (Brooks 5850E, Brooks Instrument). The feed ratio of $H_2O/(CH_4 + CO + CO_2)$ was set to 2.0. The intrinsic activity of the synthesized catalysts was evaluated at a

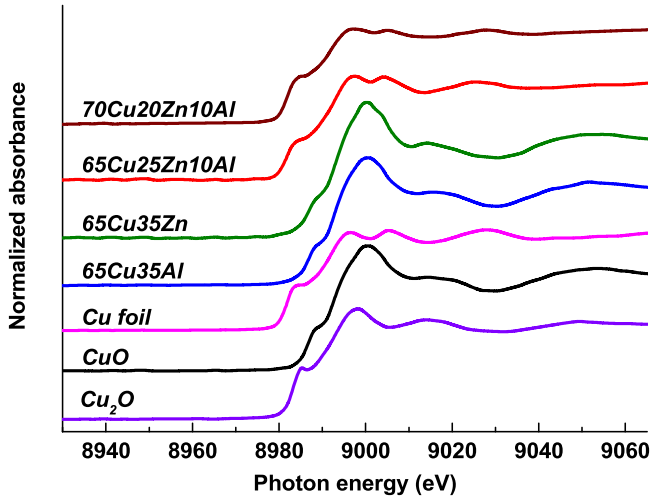

Fig. 6. Cu K-edge XANES spectra of CZA catalysts depending on Cu contents.

gas hourly space velocity (GHSV) of 8,000 mL/g·h and a temperature range of 200–240 °C. The water vapor required for the WGS reaction was supplied using a syringe pump. H_2O injected into the syringe pump was converted into a vapor phase by heating to 180 °C with a preheater located at the top of the feed gas inlet of the fixed-bed microtubular reactor. The residual moisture in the product gas was condensed and completely removed using a moisture trap combined with a chiller. The compositions of the effluent gas were analyzed with an on-line micro-gas chromatography (Micro GC Fusion® gas analyzer, INFICON) equipped with a thermal conductivity detector (TCD). The CO conversion and selectivity to CH_4 and CO_2 in the product gas were calculated by employing the following equations:

$$\text{CO conversion}(\%) = \frac{[\text{CO}]_{in} - [\text{CO}]_{out}}{[\text{CO}]_{in}} \times 100$$

$$\text{CO}_2\text{seletivity}(\%) = \frac{[\text{CO}_2]_{out} - [\text{CO}_2]_{in}}{([\text{CH}_4]_{out} - [\text{CH}_4]_{in}) + ([\text{CO}_2]_{out} - [\text{CO}_2]_{in})} \times 100$$

$$\text{CH}_4\text{seletivity}(\%) = \frac{[\text{CH}_4]_{out} - [\text{CH}_4]_{in}}{([\text{CH}_4]_{out} - [\text{CH}_4]_{in}) + ([\text{CO}_2]_{out} - [\text{CO}_2]_{in})} \times 100$$

The turnover frequency (TOF) was calculated using the following equation:

$$TOF = \frac{([\text{CO}]_{in} - [\text{CO}]_{out})AB_M F}{D_M W X_M}$$

where $[\text{CO}]_{in}$ and $[\text{CO}]_{out}$ are the inlet and outlet concentrations of CO, respectively; AB_M is the molar mass of active metal; F is the total flow rate ($mol \cdot s^{-1}$); D_M is the dispersion of active metal; W is the mass of catalyst (g_{cat}); and X_M is the content of active metal ($g_M \cdot g_{cat}^{-1}$).

3. Results and discussion

3.1. Catalyst characterization

To investigate the structural and morphological properties according to various Cu loading and support materials, SEM with EDS mappings were performed. As shown in Fig. 1, all prepared catalysts showed irregular spherical particles. Especially, 65Cu35Al showed an additional radial spine-shaped morphology. There was no significant morphological change in the samples after WGS reaction, but an average increase in particle size was observed. The EDS mapping results revealed that Cu, Zn, and Al were finely dispersed in all catalysts regardless of the amount of Cu loading, and carbon deposition did not occur according to the reaction.

In general, it is well known that Cu is very sensitive to an oxidizing atmosphere [9]. *In-situ* XRD analysis was performed to avoid Cu oxidation in the analytical conditions and to confirm the exact crystal structures of the catalysts in the activation step. As displayed in Fig. 2, all synthesized catalysts show diffraction peaks of crystalline CuO [PDF-ICDD 48-1548] and ZnO [PDF-ICDD 89-1397] in a 2 vol.% H_2/N_2 atmosphere below 200 °C. [8,10]. At 250 °C, the diffraction peaks corresponding to CuO disappeared, and the diffraction peaks corresponding to Cu [PDF-ICDD 04-0836] appeared clearly, suggesting that the pre-reduction condition in this study is sufficient to completely reduce CuO to metallic Cu [11–13].

HR-TEM analysis was conducted to further verify the exposed crystal planes of the catalysts during WGS (Fig. 3). In accordance with *in-situ* XRD results, Cu {111} plane with interplanar distance of ~ 0.210 nm and ZnO {101} plane with interplanar distance of ~ 0.248 nm were mainly observed. Additionally, interplanar distance of ~ 0.180 nm corresponding to Cu {200}, interplanar distance of ~ 0.282 nm corresponding to ZnO {100}, and interplanar distance of ~ 0.147 nm corresponding to ZnO {103} planes were observed [7,11,14,15]. No crystal plane corresponding to CuO was observed.

Table 1 described the basic characteristics of the synthesized catalysts. The specific surface area was strongly affected by the contents of Al_2O_3. Therefore, the 65Cu35Al catalyst with the highest Al_2O_3 contents (35 %) showed the highest specific surface area (138.9 m^2/g). Catalysts with a higher specific surface area generally have better catalytic performance because more surface-active sites are exposed to the reactants [16]. On the contrary, 65Cu35Zn without Al_2O_3 showed the lowest specific surface area (25.5 m^2/g). These results suggest that the addition of Al_2O_3 plays a major role in improving the specific surface area of the catalysts. Interestingly, the CZA catalyst containing a relatively small amount of Al_2O_3 (10 %) showed a significantly high specific surface area regardless of the amount of Cu supported. Since Cu has a weak property to sintering, a high dispersion strategy has become a major issue in recent catalyst research. The Cu dispersions of CZA catalysts with different Cu contents were estimated by N_2O-titration, and the results are shown in Table 1. All CZA catalysts exhibited about twice as high Cu dispersion compared to CA catalysts, despite a relatively low specific surface area. This can be ascribed as beneficial effect of ZnO–Al_2O_3 matrix effect. Al_2O_3 can act as a textural promoter or spacer, and ZnO can act as a dispersion agent [17–19]. 70Cu20Zn10Al and 65Cu25Zn10Al catalysts showed highest Cu dispersion (1.12 %) among the synthesized catalysts and decreased in the following order: 70Cu20Zn10Al, 65Cu25Zn10Al (1.12 %) > 60Cu30Zn10Al (0.95 %) > 50Cu40Zn10Al (0.89 %) > 65Cu35Al (0.55 %) > 65Cu35Zn (0.42 %). Cu particle size shows an opposite trend with the Cu dispersion. The Cu particle size increased in the following order: 70Cu20Zn10Al (77.6 nm) < 65Cu25Zn10Al (77.9 nm) < 60Cu30Zn10Al (91.8 nm) < 50Cu40Zn10Al (98.2 nm) < 65Cu35Al (158.7 nm) > 65Cu35Zn (208.7 nm).

Since the WGS reaction is an oxidation-reduction reaction, the reduction properties of Cu-based catalysts, which are particularly susceptible to oxidation, can be a major hint in identifying factors affecting catalytic performance. Fig. 4 illustrates the TPR patterns of synthesized CZA catalysts with various Cu contents. All synthesized catalysts showed similar two reduction peaks in the range of 150–250 °C. The first low temperature peak ascribed to a reduction of Cu^{2+} to Cu^{+}. The second high temperature peak can be assigned to a reduction of Cu^{+} to Cu^{0} [17, 20–24]. Compared with 65Cu35Al, 65Cu35Zn showed a reduction peak at a lower temperature, confirming that Zn improved the reducibility of Cu. In addition, ternary CZA catalysts showed higher reducibility than binary Cu–Zn or Cu–Al systems. This phenomenon is attributed to the formation of highly dispersed CuO on ZnO due to the interaction between Cu and ZnO. Furthermore, this effect is amplified by Al_2O_3 acting as a spacer.

XPS analysis was performed to confirm the chemical state of the synthesized catalyst and the distribution of surface Cu species. As shown

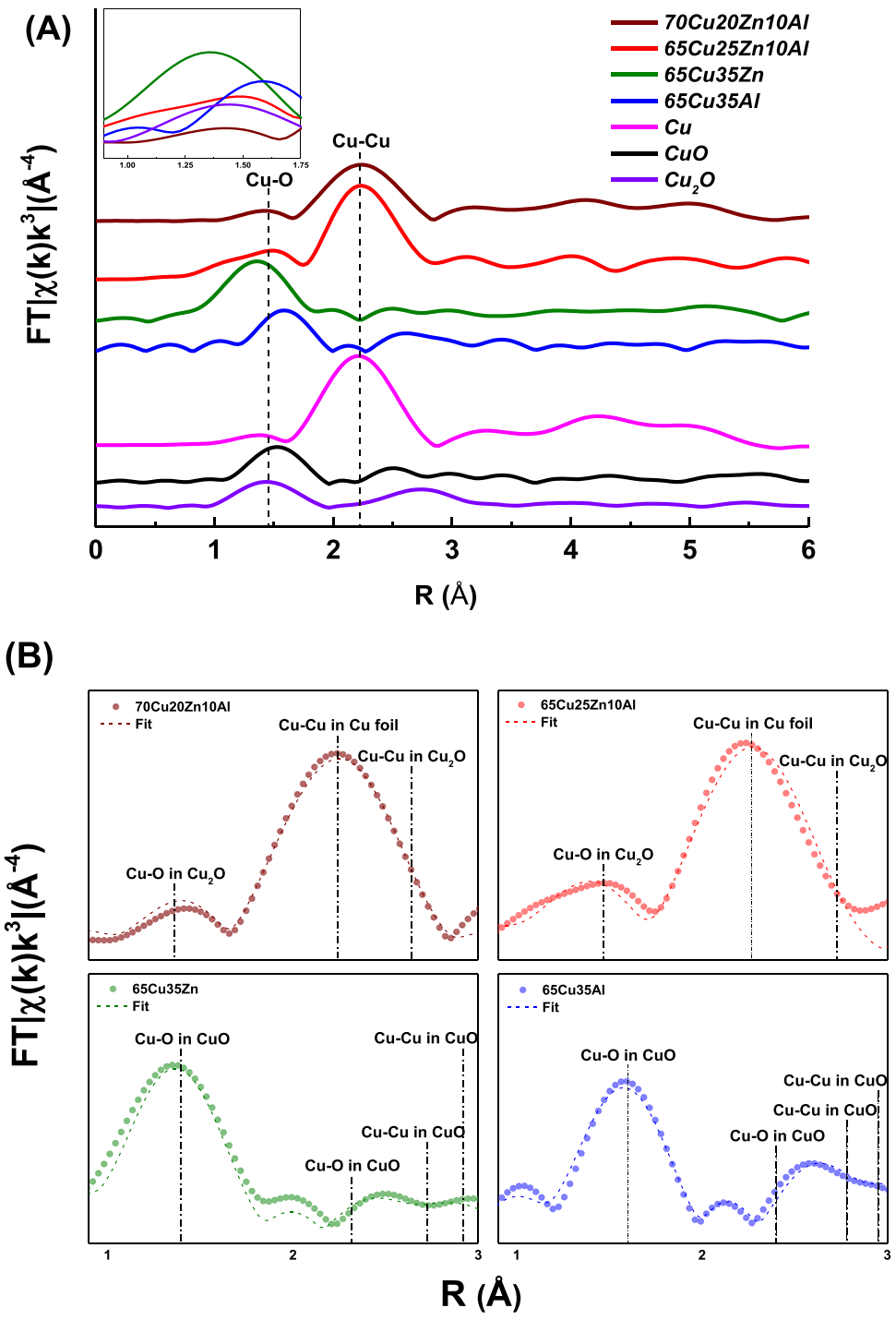

Fig. 7. Fourier transform (FT) magnitudes of k^3-weighted EXAFS spectra of CZA catalysts depending on Cu contents: (A) Normalized, and (B) Fitted.

in Fig. 5 (A), all synthesized catalysts showed characteristic peaks at 932, and 952 eV. According to the previous studies [15,25–28], peaks centered at 932 and 952 eV are defined as Cu $2p_{3/2}$ and Cu $2p_{1/2}$ binding energies, and are assigned to reduced Cu species (Cu^0, Cu^+). This result suggests that Cu^+ and Cu^0 coexist in the reduced catalysts. In particular, for catalysts with ZnO content greater than 30 %, both peaks shifted to higher binding energies. This phenomenon implies that the amount of ZnO can modify the chemical state of surface Cu species. To further confirm the valence state of reduced Cu species, the Cu LMM Auger electron spectroscopies were conducted. As shown in Fig. 5 (B), the Cu valence state of all the reduced catalysts was mainly Cu^0. The observed Cu LMM Auger spectra can be deconvoluted into two peaks. The peak centered at 570 eV is characteristic of Cu^0. The peak centered at 575 eV is characteristic of Cu^+ [29–31]. The relative ratios of Cu^0 and Cu^+, calculated from the area of each peak for the fitted Cu LMM spectra, are shown in Table 2. As indicated in Table 2, the $Cu^+/(Cu^+ + Cu^0)$ ratio was varied according to the Cu content and the support material, and 65Cu25Zn10Al exhibited the highest value. The $Cu^+/(Cu^+ + Cu^0)$ ratio decreased in the following order: 65Cu25Zn10Al (0.35) > 60Cu30Zn10Al (0.31) > 50Cu40Zn10Al, 65Cu35Zn (0.30) > 65Cu35Al (0.28) > 70Cu20Zn10Al (0.25). Notably, in the case of 70Cu20Zn10Al, despite the lowest $Cu^+/(Cu^+ + Cu^0)$ ratio, it exhibited the second highest surface Cu^+ number by the highest number of surface Cu atoms.

For further confirmation of the role of each active Cu species and the

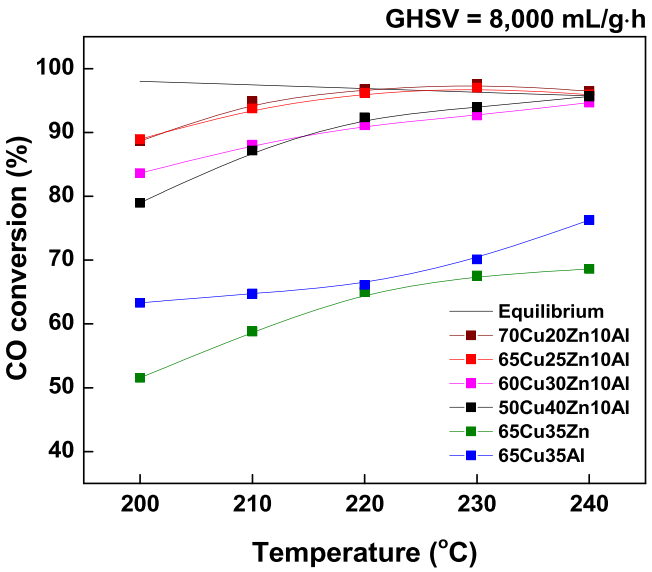

Fig. 8. CO conversion with reaction temperature over CZA catalysts depending on Cu contents ($H_2O/(CH_4 + CO + CO_2) = 2.0$; GHSV = 8,000 mL/g·h).

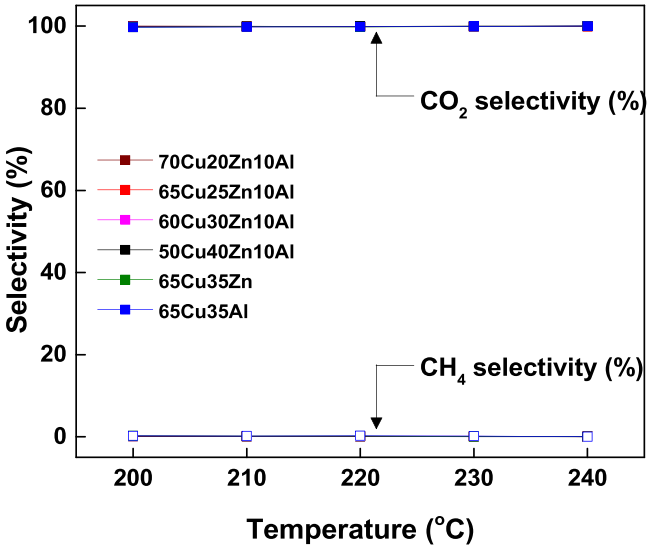

Fig. 9. CO_2 and CH_4 selectivity as a function of reaction temperature over CZA catalysts depending on Cu contents ($H_2O/(CH_4 + CO + CO_2) = 2.0$; GHSV = 8,000 mL/g·h).

location of Cu^+ by local coordination structure analysis, XAFS technique was applied. The Cu K-edge XANES spectra for CZA catalysts depending on Cu contents with Cu foil, Cu_2O and CuO as the references are shown in Fig. 6. The metallic Cu foil shows the edge absorption at 8983 eV and a doublet in the white line. The CuO shows a weak absorption peak of the pre-edge line representing the dipole-forbidden 1s → 3d electronic transition, a shoulder peak representing the 1s → $4p_z$ electron transition, and an intense absorption peak of the white line representing the 1s → $4p_{xy}$ electron transition at 8978, 8987 and 8998 eV, respectively [10]. In the case of Cu_2O, weak absorption peak at 8984 eV which corresponds to 1s–4p transition was observed. This absorption peak indicates the linear two-coordinate structure [32]. Notably, 70Cu20Zn10Al and 65Cu25Zn10Al catalysts did not showed an isosbestic point in the XANES spectra indicates the presence of more than two species during the activation step [33]. Therefore, 70Cu20Zn10Al and 65Cu25Zn10Al are considered to have a similar coordination structure because they show a shape similar to that of Cu^0 or Cu_2O.

Fig. 7 shows the normalized Fourier transform (FT) magnitudes of k^3-weighted EXAFS for CZA catalysts depending on Cu contents. Ternary system catalysts featured an intense peak indicating the first shell of Cu–Cu contribution at the range of 1.7–2.7 Å. Otherwise, binary system catalysts showed an intense peak indicating the first shell of Cu–O contribution at the range of 1.2–2.0 Å. This indicates that Cu^{2+} species and reduced Cu species predominate in binary catalysts and ternary catalysts, respectively. It is noteworthy that the position of the peak representing the Cu–O contribution of the first shell of ternary catalysts is similar to that of 65Cu35Zn and Cu_2O. Thus, it can be inferred that Cu^+ species are generated and located at the interface between Cu and Zn. Several researchers have also reported on the formation of Cu^+ at the Cu-Zn interface [8,34]. The close proximity of Cu and Zn allows Zn to act as an electron donor and generate more Cu^+ in the catalyst [34].

The local structure and structural parameters of CZA catalysts, and the fittings of coordination shells were performed. Fig. 7 (B) shows the best fit results and the structural parameters (e.g., coordination number (CN), interatomic distance (R), and Debye-Waller factor (σ^2)) are shown in Table 4. As ternary catalysts (70Cu20Zn10Al and 65Cu25Zn10Al) exhibited similar patterns of XANES spectra with Cu_2O and metallic Cu, these two compounds was used as a model for the fitting. For similar reason, CuO was selected as a model compound for binary system catalysts. Due to the low signal-to-noise level above 3.0 Å, fitting was conducted at the range of 1.2 to 3.0 Å. The overall coordination number of Cu–Cu shell for all prepared samples ranged from 8–10. A value in this range has been reported to be a nanoparticle of about 3 nm [35]. It is well known that the size of the nanoparticle increases as the saturated Cu–Cu coordination number increases [36,37]. Total coordination number of Cu–Cu contribution is increased in following order: 70Cu20Zn10Al (8.46) < 65Cu25Zn10Al (9.00) < 65Cu35Al (9.60) < 65Cu35Zn (10.40). Thus, it can be concluded that the dispersion of Cu may decrease in following order: 70Cu20Zn10Al > 65Cu25Zn10Al > 65Cu35Al > 65Cu35Zn. This result is in agreement with the trend with N_2O-titration results. In addition, the interatomic distance of the Cu–O scattering path of the first shell showed similar values for ternary system catalysts, Cu-Zn, and Cu_2O. Therefore, judging from the fitting results, it can be seen that Cu^+ is advantageously formed at the Cu-Zn interface.

3.2. *Catalytic performance*

The results of intrinsic catalytic activity tests are depicted in Fig. 8. 70Cu20Zn10Al showed the highest CO conversion within the whole temperature range, whereas 65Cu35Zn showed the lowest CO conversion below 60 %. CZA catalysts exhibited significant difference in reaction results depending on the Cu contents and thus altered behavior of Cu active sites by changing composition had a close interrelation with the catalytic activity. Reaction results revealed that the main factor affecting catalytic activity was the amounts of active species as identified by N_2O-titration [10]. In contrast, the significantly lower catalytic activity of the 65Cu35Zn is mainly induced by the lowest specific surface area and lower content of active species. Fig. 9 shows the results of calculating CO_2 and CH_4 selectivity as a function of the reaction temperature over CZA catalysts depending on Cu contents to examine the possibility of side reactions. Methanation is one of the main side reactions that occur during WGS, and since it consumes an excess H_2 and lowers the H_2 yield, it must be considered when designing the WGS catalyst [10,38,39]. All synthesized CZA catalysts exhibited 100 % CO_2 selectivity over the entire temperature range, thus proving that they are suitable catalysts for WGS that selectively convert CO into CO_2 without side reactions.

Relationship between catalytic activity, number of active species and TOF is summarized in Fig. 10 and Table 3. CO conversion was correlated to the estimated Cu active species with or without Cu^+ consideration. First of all, the binary system of Cu–ZnO and Cu–Al_2O_3 showed the low amount of Cu active species, resulting in the low CO conversion. Clearly, the ternary system of CZA exhibited the higher amount of Cu active

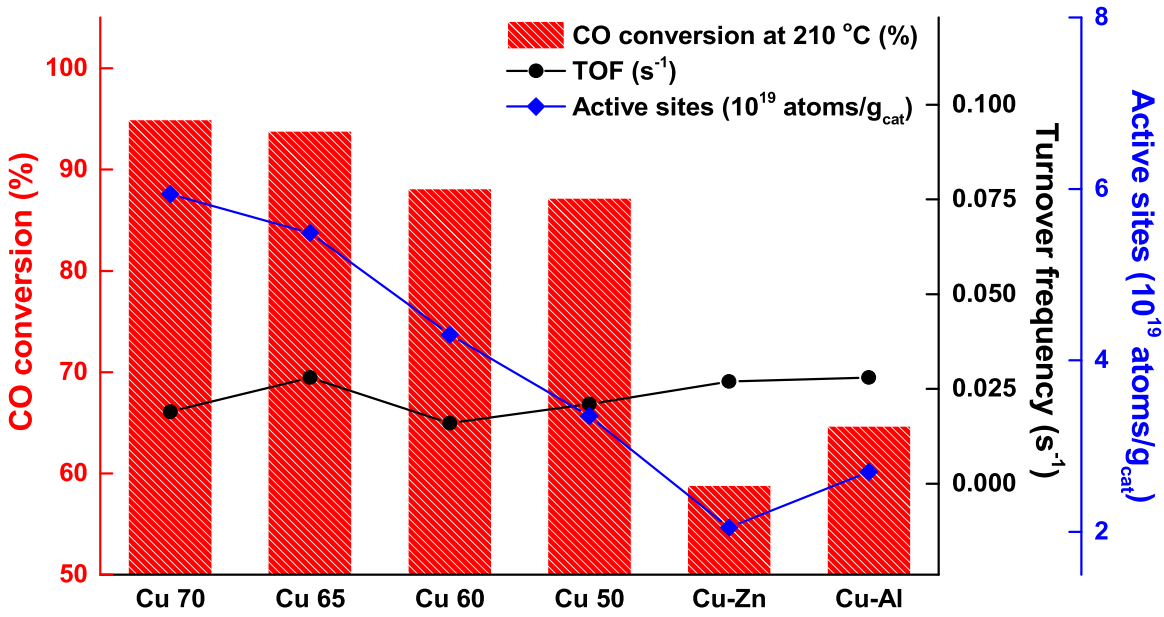

Fig. 10. Relationship between CO conversion, Cu active sites, and turnover frequency in WGS reaction depending on Cu content (Activity test – $T = 210$ °C; $H_2O/(CH_4 + CO + CO_2) = 2.0$; GHSV = 8,000 mL/g·h / TOF test – $T = 160$ °C; $H_2O/(CH_4 + CO + CO_2) = 2.0$; GHSV = 32,000 mL/g·h).

Table 3
Active sites and turnover frequency of CZA catalysts depending on Cu contents.

Description	CO conversion (%)[a]			TOF (s^{-1})[a]		Active sites (10^{19} atoms/g_{cat})
	160 °C	170 °C	210 °C	160 °C	170 °C	
70Cu20Zn10Al	7.3	12.5	94.9	0.019	0.032	5.94
65Cu25Zn10Al	10.0	12.9	93.8	0.028	0.036	5.49
60Cu30Zn10Al	4.5	7.3	88.1	0.016	0.026	4.30
50Cu40Zn10Al	4.6	8.6	87.2	0.021	0.039	3.35
65Cu35Zn	3.6	4.7	58.8	0.027	0.035	2.05
65Cu35Al	5.0	8.9	64.7	0.028	0.051	2.70

[a] $T = 160 – 170$ °C, $P = 1$ atm, GHSV = 32,000 mL/g·h, CO conversion < 20 %.

species and CO conversion than the those of the binary system. As shown in Fig. 10, the CO conversion increased linearly with the number of active species. In contrast, the TOF value showed a constant value (ca. 0.024 s^{-1}) regardless of the Cu contents. Fig. 11 shows the TOF value as a function of Cu dispersion. The TOF value was maintained at a constant value without dependence on Cu dispersion. Therefore, it can be concluded that the CZA catalyst is structure-insensitive in WGS.

In particular, both 65Cu25Zn10Al and 70Cu20Zn10Al catalysts showed the higher CO conversion compared to the others. However, it is interesting to note that the CO conversion of 70Cu20Zn10Al was similar to that of 65Cu25Zn10Al, which possessed a smaller amount of Cu active species than 70Cu20Zn10Al. Thus, it is necessary to compare the activity to the amount of Cu active species considering the Cu^+. Fig. 12 shows the CO conversion as a function of the number of surface Cu^+ species. CO conversion was clearly increased linearly with the number of surface Cu^+ species.

To compare the durability of 65Cu25Zn10Al and 70Cu20Zn10Al catalysts, LT-WGS was carried out at 240 °C and a GHSV of 16,000 mL/g·h. As shown in Fig. 13, the initial CO conversion of 70Cu20Zn10Al was higher than that of 65Cu25Zn10Al, but it decreased slightly after 3 h of reaction and thereafter showed a decreasing tendency. On the other hand, 65Cu25Zn10Al showed high stability and maintained high CO

Table 4
EXAFS fitting results of CZA catalysts depending on Cu contents.

Model	Scattering path	*CN*	*R* (Å)	σ^2 ($Å^2 \times 10^{-3}$)
CuO	Cu–O	4	1.956	–
	Cu–O	2	2.784	–
	Cu–Cu	4	2.901	–
	Cu–Cu	4	3.083	–
Cu_2O	Cu–O	2	1.849	–
	Cu–Cu	12	3.019	–
Cu	Cu–Cu	12	2.553	–

Sample	Selected Model	Scattering path	*CN*	*R* (Å)	σ^2 ($Å^2 \times 10^{-3}$)
70Cu20Zn10Al	Cu_2O	Cu–O	1.00	1.77 ± 0.066	6.40 ± 4.3
		Cu–Cu	0.66	3.04 ± 0.075	12.2 ± 9.6
	Cu	Cu–Cu	7.80	2.55 ± 0.009	10.6 ± 0.4
65Cu25Zn10Al	Cu_2O	Cu–O	0.30	1.86 ± 0.080	9.96 ± 2.5
		Cu–Cu	1.80	3.03 ± 0.021	6.08 ± 0.9
	Cu	Cu–Cu	7.20	2.56 ± 0.015	5.82 ± 0.8
65Cu35Zn	CuO	Cu–O	6.52	1.86 ± 0.008	4.64 ± 0.5
		Cu–O	3.26	2.67 ± 0.018	5.28 ± 2.2
		Cu–Cu	5.20	2.97 ± 0.022	6.59 ± 1.2
		Cu–Cu	5.20	3.15 ± 0.005	6.44 ± 0.5
65Cu35Al	CuO	Cu–O	3.20	1.98 ± 0.008	2.48 ± 0.5
		Cu–O	1.60	2.82 ± 0.022	3.96 ± 2.8
		Cu–Cu	4.80	3.04 ± 0.019	7.20 ± 1.2
		Cu–Cu	4.80	3.22 ± 0.005	7.73 ± 0.6

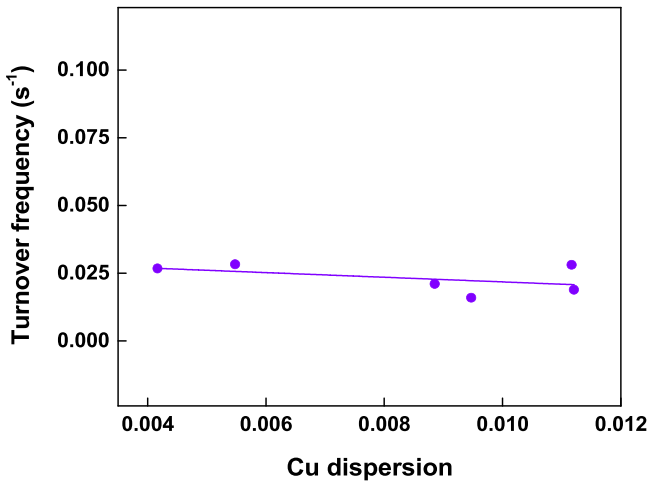

Fig. 11. TOF results as a function of Cu dispersion (T = 160 °C; $H_2O/(CH_4 + CO + CO_2)$ = 2.0; GHSV = 32,000 mL/g·h).

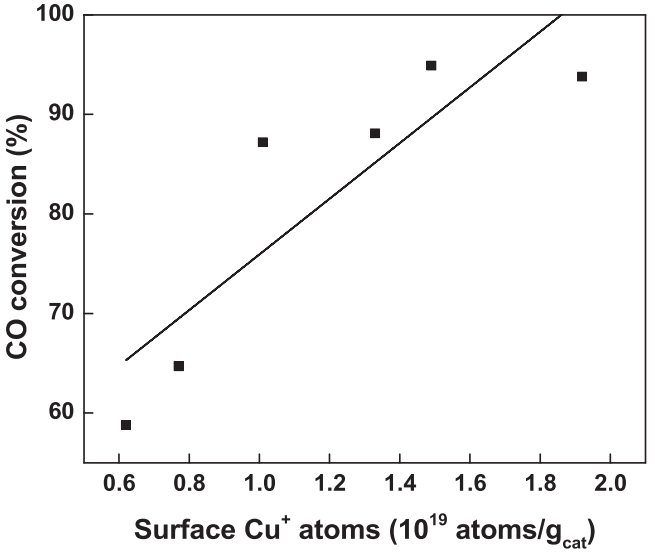

Fig. 12. CO conversion as a function of number of surface Cu^+ species (T = 210 °C; $H_2O/(CH_4 + CO + CO_2)$ = 2.0; GHSV = 8,000 mL/g·h).

conversion for 200 h without deactivation.

To confirm the stability of the 65Cu25Zn10Al catalysts, TEM with particle size distribution analysis was conducted, as shown in Fig. 14. The 70Cu20Zn10Al catalyst showed a relatively uniform particle size distribution, and the particle size of the reduced sample was also smaller than that of the 65Cu25Zn10Al catalyst. However, in the case of the used sample, the average particle size increased by about 2 times to 50 nm, indicating that it was vulnerable to sintering. The *ex-situ* XRD patterns of used 70Cu20Zn10Al and 65Cu25Zn10Al catalysts (Fig. S1) confirmed that these catalysts remain in the reduced states, even after 24 h of reaction, without observable differences from the *in-situ* XRD results in Fig. 2. However, the number of active sites ($Cu^0 + Cu^+$) calculated from N_2O-titration results and Cu LMM spectra of used 70Cu20Zn10Al and 65Cu25Zn10Al catalysts (Table S1 and Fig. S2) revealed the vulnerability of 70Cu20Zn10Al to Cu sintering. The number of Cu surface atoms of 70Cu20ZnAl was reduced by about 25 % after 24 h of reaction compared to that of the fresh catalyst (Fresh: 5.94 × 10^{19} atoms/g_{cat} / Used: 4.45 × 10^{19} atoms/g_{cat}). 65Cu25Zn10Al also showed similar results with about 21 % decrease, but there was a clear difference in the

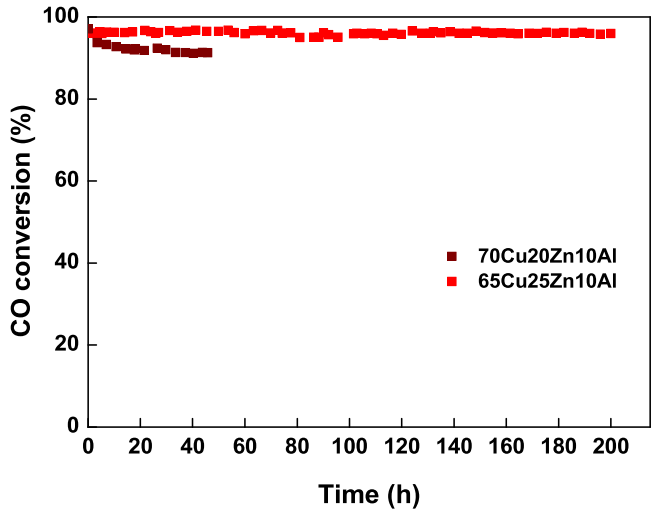

Fig. 13. CO conversion with time on stream over the 65Cu25Zn10Al and 70Cu20Zn10Al catalysts ($H_2O/(CH_4 + CO + CO_2)$ = 2.0; T = 240 °C; GHSV = 16,000 mL/g·h).

number of surface Cu^+ atoms. 65Cu25Zn10Al showed a decrease of only 9.9 %, but 70Cu20Zn10Al showed a decrease of 12.8 %, indicating that Cu^+ contributes significantly to the stability of the catalyst during WGS. This can be explained by the reaction mechanism and major role of Cu^+ in WGS. The WGS reaction occurs via a redox cycle between $Cu^0 \leftrightarrow Cu^+$, in which Cu^+ sites oxidize chemisorbed CO to CO_2 and turn into Cu^0. After that, the reduced Cu^0 sites are re-oxidized by H_2O to produce H_2 and turn into Cu^+ [40,41]. Therefore, it can be said that the presence of surface Cu^+ atoms can protect and assist Cu^0, which is vulnerable to sintering, in the WGS environment where oxidation-reduction occurs continuously.

As a result, 65Cu25Zn10Al showed the best catalytic activity and the similar catalytic performance compared to 70Cu20Zn10Al because of its highly active Cu^+ species despite the lower amount of Cu active species than 70Cu20Zn10Al. Moreover, the lower content of Cu with highly active Cu^+ species can have a benefit for the strong resistance to sintering which is well-known for the main drawback of Cu-based catalysts.

4. Conclusions

To specify the active species of the CZA catalyst and to verify the structure sensitivity, Cu loading was systematically changed. 65Cu35Al exhibited higher specific surface area than CZA, confirming that Al had a beneficial effect on the specific surface area of the catalyst. On the other hand, 65Cu35Zn showed easier reducibility than 65Cu35Al, confirming that the addition of Zn improves the reducibility. In particular, the ternary CZA catalyst exhibited easier reducibility and a relatively high specific surface area compared to the binary Cu–Zn and Cu–Al catalysts due to the synergistic effect of Zn and Al. The intrinsic activity tests revealed that the most critical factor is the number of active sites. As a consequence, 70Cu20Zn10Al with the highest number of active sites showed the highest CO conversion. From TOF results, all the catalysts showed constant TOF values regardless of Cu dispersion. Therefore, CZA is structure insensitive in WGS. However, the TOF value increased with increasing $Cu^+/(Cu^0 + Cu^+)$ ratio. Since 65Cu25Zn10Al has higher Cu^+ species, the CO conversion of this catalyst is similar to that of 70Cu20Zn10Al even though ($Cu^0 + Cu^+$) species of the former is less than the latter. In addition, the former showed enhanced stability due to the fact that Cu^+ species is more stable under both oxidative and reductive environment in WGS. As a result, 65 wt.% is the optimal Cu loading for WGS.

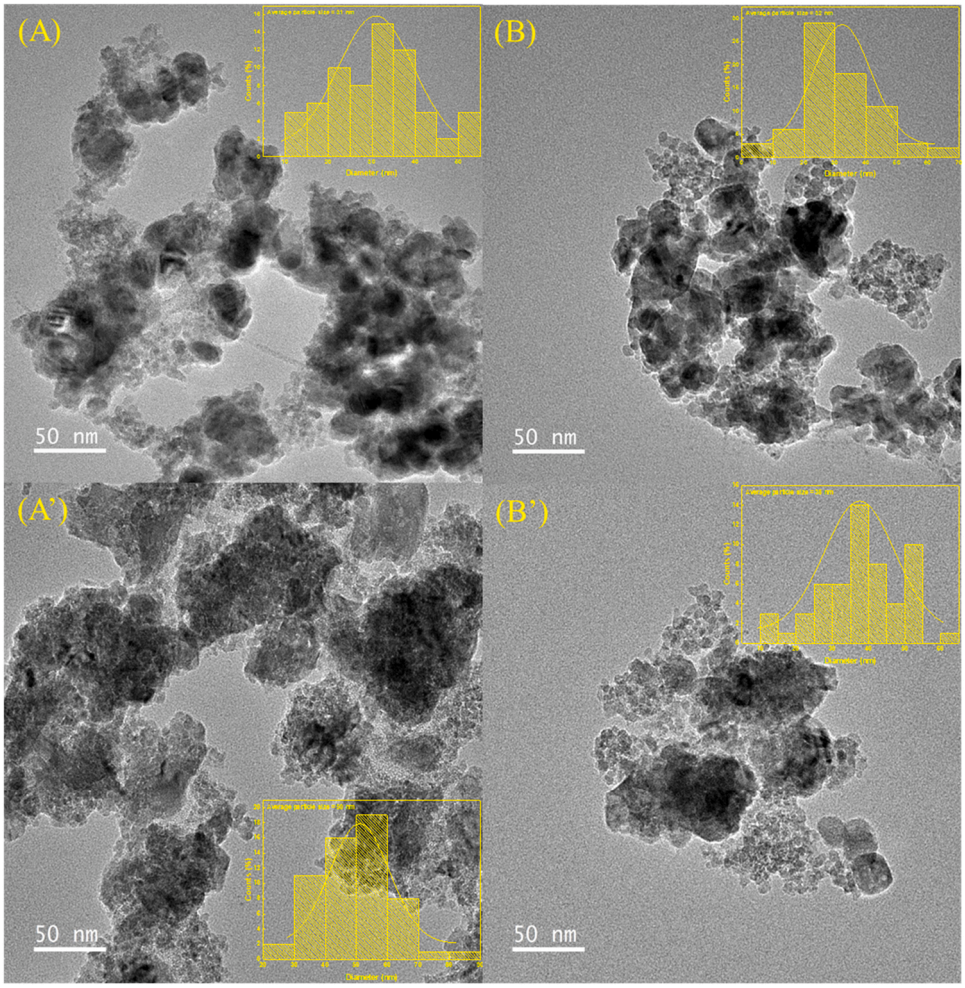

Fig. 14. TEM images of reduced and used CZA catalysts: (A) reduced 70Cu20Zn10Al, (A′) used 70Cu20Zn10Al, (B) reduced 65Cu25Zn10Al, and (B′) used 65Cu25Zn10Al.

CRediT authorship contribution statement

Seon-Yong Ahn: Conceptualization, Writing – original draft, Writing – review & editing. **Kyoung-Jin Kim:** Conceptualization, Methodology. **Beom-Jun Kim:** Data curation, Investigation. **Jae-Oh Shim:** Investigation, Supervision. **Won-Jun Jang:** Conceptualization, Supervision, Project administration. **Hyun-Seog Roh:** Conceptualization, Supervision, Funding acquisition.

Declaration of Competing Interest

The authors declare that they have no known competing financial interests or personal relationships that could have appeared to influence the work reported in this paper.

Data availability

No data was used for the research described in the article.

Acknowledgements

This work was supported by the National Research Foundation of Korea (NRF) grant funded by the Korean government (MSIT) (No. 2020R1A2B5B01002346 and 2022R1A4A1029632).

Appendix A. Supporting information

Supplementary data associated with this article can be found in the online version at doi:10.1016/j.apcatb.2022.122320.

References

[1] W.J. Jang, J.O. Shim, H.M. Kim, S.Y. Yoo, H.S. Roh, A review on dry reforming of methane in aspect of catalytic properties, Catal. Today 324 (2019) 15–26, https://doi.org/10.1016/j.cattod.2018.07.032.
[2] P. Gawade, B. Mirkelamoglu, U.S. Ozkan, The role of support morphology and impregnation medium on the water gas shift activity of ceria-supported copper catalysts, J. Phys. Chem. C 114 (2010) 18173–18181, https://doi.org/10.1021/jp104715w.
[3] P. Guo, L. Chen, Q. Yang, M. Qiao, H. Li, H. Li, H. Xu, K. Fan, Cu/ZnO/Al_2O_3 water-gas shift catalysts for practical fuel cell applications: the performance in shut-down/start-up operation, Int. J. Hydrog. Energy 34 (2009) 2361–2368, https://doi.org/10.1016/j.ijhydene.2008.12.081.
[4] D. Li, Y. Cai, Y. Ding, R. Li, M. Lu, L. Jiang, Layered double hydroxides as precursors of Cu catalysts for hydrogen production by water-gas shift reaction, Int. J. Hydrog. Energy 40 (2015) 10016–10025, https://doi.org/10.1016/j.ijhydene.2015.05.183.
[5] M.J.L. Ginés, N. Amadeo, M. Laborde, C.R. Apesteguía, Activity and structure-sensitivity of the water-gas shift reaction over Cu–Zn–Al mixed oxide catalysts, Appl. Catal. A Gen. 131 (1995) 283–296, https://doi.org/10.1016/0926-860X(95)00146-8.
[6] H. Yan, X.T. Qin, Y. Yin, Y.F. Teng, Z. Jin, C.J. Jia, Promoted Cu-Fe_3O_4 catalysts for low-temperature water gas shift reaction: optimization of Cu content, Appl. Catal. B Environ. 226 (2018) 182–193, https://doi.org/10.1016/j.apcatb.2017.12.050.
[7] Z. Cui, S. Song, H. Liu, Y. Zhang, F. Gao, T. Ding, Y. Tian, X. Fan, X. Li, Synergistic effect of Cu^+ single atoms and Cu nanoparticles supported on alumina boosting water-gas shift reaction, Appl. Catal. B Environ. 313 (2022), 121468, https://doi.org/10.1016/j.apcatb.2022.121468.

[8] Z. Zhang, X. Chen, J. Kang, Z. Yu, J. Tian, Z. Gong, A. Jia, R. You, K. Qian, S. He, B. Teng, Y. Cui, Y. Wang, W. Zhang, W. Huang, The active sites of Cu–ZnO catalysts for water gas shift and CO hydrogenation reactions, Nat. Commun. 12 (2021) 6–14, https://doi.org/10.1038/s41467-021-24621-8.

[9] M.V. Twigg, M.S. Spencer, Deactivation of supported copper metal catalysts for hydrogenation reactions, Appl. Catal. A Gen. 212 (2001) 161–174, https://doi.org/10.1016/S0926-860X(00)00854-1.

[10] S.Y. Ahn, H.S. Na, K.W. Jeon, Y.L. Lee, K.J. Kim, J.O. Shim, H.S. Roh, Effect of Cu/CeO_2 catalyst preparation methods on their characteristics for low temperature water−gas shift reaction: a detailed study, Catal. Today 352 (2020) 166–174, https://doi.org/10.1016/j.cattod.2019.11.017.

[11] X. Dong, Z. Wang, Y. Yuan, Y. Yang, Synergistic catalysis of Cu+/Cu0 for efficient and selective N-methylation of nitroarenes with para-formaldehyde, J. Catal. 375 (2019) 304–313, https://doi.org/10.1016/j.jcat.2019.06.022.

[12] D. Li, S. Xu, Y. Cai, C. Chen, Y. Zhan, L. Jiang, Characterization and catalytic performance of Cu/ZnO/Al2O3 water-gas shift catalysts derived from Cu-Zn-Al layered double hydroxides, Ind. Eng. Chem. Res. 56 (2017) 3175–3183, https://doi.org/10.1021/acs.iecr.6b04337.

[13] D.A. Svintsitskiy, T.Y. Kardash, O.A. Stonkus, E.M. Slavinskaya, A.I. Stadnichenko, S.V. Koscheev, A.P. Chupakhin, A.I. Boronin, In situ XRD, XPS, TEM, and TPR study of highly active in co oxidation CuO nanopowders, J. Phys. Chem. C 117 (2013) 14588–14599, https://doi.org/10.1021/jp403339r.

[14] P. Jia, Y. Liu, R. Yang, P. Luo, W. Huang, Insight into the structural sensitivity of CuZnAl catalysts for CO hydrogenation to alcohols, Fuel 323 (2022), 124265, https://doi.org/10.1016/j.fuel.2022.124265.

[15] X. Wang, K. Ma, L. Guo, Y. Tian, Q. Cheng, X. Bai, J. Huang, T. Ding, X. Li, Cu/ZnO/SiO2 catalyst synthesized by reduction of ZnO-modified copper phyllosilicate for dimethyl ether steam reforming, Appl. Catal. A Gen. 540 (2017) 37–46, https://doi.org/10.1016/j.apcata.2017.04.013.

[16] J.O. Shim, D.W. Jeong, W.J. Jang, K.W. Jeon, S.H. Kim, B.H. Jeon, H.S. Roh, J. G. Na, Y.K. Oh, S.S. Han, C.H. Ko, Optimization of unsupported CoMo catalysts for decarboxylation of oleic acid, Catal. Commun. 67 (2015) 16–20, https://doi.org/10.1016/j.catcom.2015.03.034.

[17] R.T. Figueiredo, H.M.C. Andrade, J.L.G. Fierro, Influence of the preparation methods and redox properties of Cu/ZnO/Al_2O_3 catalysts for the water gas shift reaction, J. Mol. Catal. A Chem. 318 (2010) 15–20, https://doi.org/10.1016/j.molcata.2009.10.028.

[18] A.A.G. Lima, M. Nele, E.L. Moreno, H.M.C. Andrade, Composition effects on the activity of Cu-ZnO-Al2O3 based catalysts for the water gas shift reaction: a statistical approach, Appl. Catal. A Gen. 171 (1998) 31–43, https://doi.org/10.1016/S0926-860X(98)00072-6.

[19] T. Fujitani, M. Saito, Y. Kanai, T. Kakumoto, T. Watanabe, J. Nakamura, T. Uchijima, The role of metal oxides in promoting a copper catalyst for methanol synthesis, Catal. Lett. 25 (1994) 271–276, https://doi.org/10.1007/BF00816307.

[20] H.S. Na, S.Y. Ahn, J.O. Shim, K.W. Jeon, H.M. Kim, Y.L. Lee, W.J. Jang, B.H. Jeon, H.S. Roh, Effect of precipitation on physico-chemical and catalytic properties of Cu-Zn-Al catalyst for water-gas shift reaction, Korean J. Chem. Eng. 36 (2019) 1243–1248, https://doi.org/10.1007/s11814-019-0309-8.

[21] R.-X. Zhou, X.-Y. Jiang, J.-X. Mao, X.-M. Zheng, Oxidation of carbon monoxide catalyzed composite oxides by manganese-silver, Appl. Catal. A Gen. 162 (1997) 213–222.

[22] G. Águila, F. Gracia, J. Cortés, P. Araya, Effect of copper species and the presence of reaction products on the activity of methane oxidation on supported CuO catalysts, Appl. Catal. B Environ. 77 (2008) 325–338, https://doi.org/10.1016/j.apcatb.2007.08.002.

[23] K.V.R. Chary, G.V. Sagar, C.S. Srikanth, V.V. Rao, Characterization and catalytic functionalities of copper oxide catalysts supported on zirconia, J. Phys. Chem. B 111 (2007) 543–550, https://doi.org/10.1021/jp063335x.

[24] C.Z. Yao, L.C. Wang, Y.M. Liu, G.S. Wu, Y. Cao, W.L. Dai, H.Y. He, K.N. Fan, Effect of preparation method on the hydrogen production from methanol steam reforming over binary Cu/ZrO2 catalysts, Appl. Catal. A Gen. 297 (2006) 151–158, https://doi.org/10.1016/j.apcata.2005.09.002.

[25] J.O. Shim, H.S. Na, A. Jha, W.J. Jang, D.W. Jeong, I.W. Nah, B.H. Jeon, H.S. Roh, Effect of preparation method on the oxygen vacancy concentration of CeO_2-promoted Cu/γ-Al_2O_3 catalysts for HTS reactions, Chem. Eng. J. 306 (2016) 908–915, https://doi.org/10.1016/j.cej.2016.08.030.

[26] S. Zhu, X. Gao, Y. Zhu, W. Fan, J. Wang, Y. Li, A highly efficient and robust Cu/SiO2 catalyst prepared by the ammonia evaporation hydrothermal method for glycerol hydrogenolysis to 1,2-propanediol, Catal. Sci. Technol. 5 (2015) 1169–1180, https://doi.org/10.1039/c4cy01148a.

[27] X. Zheng, H. Lin, J. Zheng, X. Duan, Y. Yuan, Lanthanum oxide-modified Cu/SiO2 as a high-performance catalyst for chemoselective hydrogenation of dimethyl oxalate to ethylene glycol, ACS Catal. 3 (2013) 2738–2749, https://doi.org/10.1021/cs400574v.

[28] Z. He, H. Lin, P. He, Y. Yuan, Effect of boric oxide doping on the stability and activity of a Cu-SiO 2 catalyst for vapor-phase hydrogenation of dimethyl oxalate to ethylene glycol, J. Catal. 277 (2011) 54–63, https://doi.org/10.1016/j.jcat.2010.10.010.

[29] S.Y. Ahn, K. Park, D. Choi, J. Park, Y.J. Kim, H.S. Kim, A study on the transition of copper oxide by the incorporation of nitrogen, Electron 8 (2019), https://doi.org/10.3390/electronics8101099.

[30] C. Holse, C.F. Elkjær, A. Nierhoff, J. Sehested, I. Chorkendorff, S. Helveg, J. H. Nielsen, Dynamic behavior of CuZn nanoparticles under oxidizing and reducing conditions, J. Phys. Chem. C 119 (2015) 2804–2812, https://doi.org/10.1021/jp510015v.

[31] A.C. Poulose, S. Veeranarayanan, M.S. Mohamed, R.R. Aburto, T. Mitcham, R. R. Bouchard, P.M. Ajayan, Y. Sakamoto, T. Maekawa, D.S. Kumar, Multifunctional Cu 2′x Te nanocubes mediated combination therapy for multi-drug resistant MDA MB 453, Sci. Rep. 6 (2016) 1–13, https://doi.org/10.1038/srep35961.

[32] L.S. Kau, K.O. Hodgson, E.I. Solomon, X-ray absorption edge and exafs study of the copper sites in zno methanol synthesis catalysts, J. Am. Chem. Soc. 111 (1989) 7103–7109, https://doi.org/10.1021/ja00200a032.

[33] X. Wang, J.C. Hanson, A.I. Frenkel, J.Y. Kim, J.A. Rodriguez, Time-resolved studies for the mechanism of reduction of copper oxides with carbon monoxide: complex behavior of lattice oxygen and the formation of suboxides, J. Phys. Chem. B. 108 (2004) 13667–13673, https://doi.org/10.1021/jp040366o.

[34] S. Katanyutanon, D. Samarasinghe, L. Lawtrakul, P. Toochinda, Catalytic activity enhancement of Cu-Zn-based catalyst for methanol steam reforming with magnetic inducement, Catalysts 11 (2021), https://doi.org/10.3390/catal11091110.

[35] S. Calvin, M.M. Miller, R. Goswami, S.F. Cheng, S.P. Mulvaney, L.J. Whitman, V. G. Harris, Determination of crystallite size in a magnetic nanocomposite using extended x-ray absorption fine structure, J. Appl. Phys. 94 (2003) 778–783, https://doi.org/10.1063/1.1581344.

[36] S.Y. Yao, W.Q. Xu, A.C. Johnston-Peck, F.Z. Zhao, Z.Y. Liu, S. Luo, S. D. Senanayake, A. Martínez-Arias, W.J. Liu, J.A. Rodriguez, Morphological effects of the nanostructured ceria support on the activity and stability of CuO/CeO2 catalysts for the water-gas shift reaction, Phys. Chem. Chem. Phys. 16 (2014) 17183–17195, https://doi.org/10.1039/c4cp02276a.

[37] N. Koizumi, S. Suzuki, Y. Ibi, Y. Hayasaka, Y. Hamabe, T. Shindo, M. Yamada, Mechanism for enhancing dispersion of Co 3O 4 nanoparticles in Co/SiO 2 Fischer-Tropsch synthesis catalyst by adding glycol to impregnating solution: a quick-XAFS study, J. Synchrotron Radiat. 19 (2012) 74–83, https://doi.org/10.1107/S0909049511041240.

[38] Y.L. Lee, K. Lee, C. Hyun Ko, H.S. Roh, Optimization of nano-catalysts for application in compact reformers, Chem. Eng. J. 431 (2022), 134299, https://doi.org/10.1016/j.cej.2021.134299.

[39] S.-Y. Ahn, W.-J. Jang, J.-O. Shim, B.-H. Jeon, H.-S. Roh, CeO_2-based oxygen storage capacity materials in environmental and energy catalysis for carbon neutrality: extended application and key catalytic properties, Catal. Rev. Sci. Eng. (2023) (Article in press).

[40] Y. Li, Q. Fu, M. Flytzani-Stephanopoulos, Low-temperature water-gas shift reaction over Cu- and Ni-loaded cerium oxide catalysts, Appl. Catal. B Environ. 27 (2000) 179–191, https://doi.org/10.1016/S0926-3373(00)00147-8.

[41] N.A. Koryabkina, A.A. Phatak, W.F. Ruettinger, R.J. Farrauto, F.H. Ribeiro, Determination of kinetic parameters for the water-gas shift reaction on copper catalysts under realistic conditions for fuel cell applications, J. Catal. 217 (2003) 233–239, https://doi.org/10.1016/S0021-9517(03)00050-2.